An Ab Initio Study of the Oxygen Defect Formation and Oxide Ion Migration in $(Sr_{1-x}Pr_x)_2FeO_{4\pm\delta}$

Nicholas A. Szaro[a], Salai Cheettu Ammal[a], Fanglin Chen[b], Andreas Heyden[a]*

[a] Department of Chemical Engineering, University of South Carolina, 301 South Main Street, Columbia, South Carolina 29208, United States

[b] Department of Mechanical Engineering, University of South Carolina, 300 South Main Street, Columbia, South Carolina 29208, United States

*Email: heyden@cec.sc.edu

Keywords

Ruddlesden-Popper; Mixed Ion-Electron Conductor; Solid Oxide Fuel Cell; intermediate-temperature; $(Sr_{1-x},Pr_x)_2FeO_4$

Abstract

The $Sr_{n+1}Fe_nO_{3n+1}$ Ruddlesden-Popper (RP) perovskite family displays promising oxygen permeability and serves as a host stoichiometry for the design of solid oxide electrode materials. A strategy to tune electronic and ionic properties is the introduction of substitutional dopants like Pr^{3+} to the A-site. In this study, we investigate the bulk structural, electronic, and oxygen migration properties for the n = 1 RP perovskite $(Sr_{1-x}Pr_x)_2FeO_{4\pm\delta}$ (x = 0, 0.125, 0.25, 0.375, and 0.5). The oxygen partial pressure is adjusted to elucidate how anodic and cathodic operating conditions influence the formation of oxygen defects. Under anodic conditions, the oxygen vacancy as the dominant oxide defect for all dopant-configurations. Under cathodic conditions, oxygen vacancy defects dominate for configurations from x = 0 to x = 0.375 while the oxygen peroxide interstitial defect becomes the primary defect for x = 0.5. Next, we examine the relationship between Pr^{3+} concentration, iron oxidation state, and charge compensation with defect formation to explain the trends in vacancy and peroxide interstitial formation energies. Results clarify the role of lanthanide A-site substitutional dopants on the electronic conductivity and oxide defect formation and migration in Sr-based RP perovskites. These atomic-scale insights suggest design directions for RP perovskites in SOFCs.

Keywords: Solid oxide fuel cells, Ruddlesden-Popper, oxygen migration, oxide defects

1. Introduction

Mixed ionic-electronic conducting (MIEC) materials have found use as oxygen permeation membranes and solid oxide fuel cell (SOFC) anodes and cathodes [1–3]. For SOFC applications, MIEC design is primarily focused on reducing high oxygen reduction overpotentials at the cathode and increasing the stability of the anode against coking and sulfur poisoning [4,5]. Mitigation of these losses can shift the operating temperatures of SOFCs from greater than 800 °C to the intermediate-temperature (IT) regime between 600 and 800 °C [6,7]. High temperatures facilitate fast reaction kinetics without the need for expensive metal catalysts (e.g., Pt), but cause premature aging of the SOFC stack [6,8]. While transition metal-based cubic (e.g. BSCF, LSM, and LSCF) [9–11] and double perovskites (e.g. SFMO) [12–15] have encountered widespread attention as MIEC materials in SOFCs, these materials are disadvantaged by poor ionic conductivity at low temperatures [16] and suffer from degradation at SOFC operating conditions [17,18]. In order to circumvent these difficulties, another class of perovskite materials called Ruddlesden-Popper (RP) phase oxides have been explored which display enhanced oxygen transport and promising catalytic activity for both hydrogen and hydrocarbon oxidation under high sulfur conditions [19–22].

Recent studies investigated $Sr_3Fe_2O_{7-\delta}$, the n = 2 member in the $Sr_{n+1}Fe_nO_{3n+1}$ series, as a possible cathode material [23–25] due to its excellent structural stability. A computational study by Ota et. al. [26] elucidated the relationship of vacancy defect formation and migration in $Sr_3Fe_2O_{7-\delta}$ as a function of the non-stoichiometry factor (δ) and identified defect stability with $\delta = 0.25$. The vacancy defects were found to be predominantly located between the bilayers of the FeO_2 planes. To evaluate the catalytic activity of $Sr_3Fe_2O_{7-\delta}$, Tan et. al. examined the oxygen reduction reaction (ORR) kinetics on both FeO_2 and SrO (001) surfaces and concluded that the O_2 dissociation barrier needs to be reduced to decrease kinetic losses [27]. A common strategy used to improve the

performance of such MIEC materials is to utilize substitutional dopants in order to tune the electronic, ionic, and catalytic properties. Kagomiya et al. reported that the introduction of La^{3+} lowered the vacancy migration barrier between the (Sr,La)FeO_3 perovskite layers and a change in oxide ion migration mechanism was observed at temperatures above 830 °C [24]. Here, we focus on the bulk properties of $Sr_2FeO_{4\pm\delta}$, the n = 1 member of $Sr_{n+1}Fe_nO_{3n+1}$ at the intermediate temperature regime (e.g., 800 °C). $Sr_2FeO_{4\pm\delta}$ decomposes to $Sr_3Fe_2O_{7-\delta}$ at 930 °C under atmospheric oxygen [28] and therefore, we find that it is constructive to elucidate the defect formation and migration of $Sr_2FeO_{4\pm\delta}$ as this phase is likely to coexist with $Sr_3Fe_2O_{7-\delta}$ in the intermediate temperature regime. In order to understand the effect of doping at the A-site, we further examined the bulk properties of the $(Sr_{1-x}Pr_x)_2FeO_{4-\delta}$ (SPF) material. We chose Pr^{3+} as A-site dopant because experimental studies reported that the anode material, $Pr_{0.8}Sr_{1.2}(Co,Fe)_{0.8}Nb_{0.2}O_{4+\delta}$ (PSCFN) displayed excellent oxidation kinetics, good stability under H_2S, and negligible coke formation [12,29]. Furthermore, a recent study by Tan et. al. [30] reported that the $Pr_{0.8}Sr_{1.2}(Fe,Ni)O_{4-\delta}$ (PSNF) material with exsolved NiFe nanoparticles is a promising anode material for direct hydrocarbon fuel SOFCs. We intend in this study to understand how the introduction of an A-site dopant affects the Sr_2FeO_4 series as a function of applied partial pressure of oxygen (e.g., anodic and cathodic conditions) at the interface of the IT operating regime (e.g., 1073 K).

This study utilizes density functional theory (DFT) to examine the bulk structural, electronic, and oxygen defect formation properties of SPF (x = 0, 0.125, 0.25, 0.375, and 0.5) as a function of the concentration of Pr^{3+} and oxygen partial pressure. Here, we considered all possible arrangements of Sr/Pr for a given composition within a 56-atom supercell and outlined the effects of oxygen defect formation with δ values of ± 0.125. We show that Pr^{3+} substitution strongly

influences the structural and electronic properties, oxide defect formation energies, and oxide migration barriers of the SPF family. The findings of this work, particularly the relationship of Pr^{3+} concentration and oxygen defect formation energy, provide a baseline understanding for future material design related to $(Sr_{1-x}Pr_x)_2FeO_4$ and supplement material design for other $(Sr,A)_2FeO_4$ RP perovskites.

2. Methods

Electronic energies are obtained with spin-polarized Kohn-Sham DFT+*U* calculations with periodic boundary conditions via the Vienna Ab Initio Simulation Package (VASP) [31]. Electron exchange-correlation effects were evaluated by utilizing the generalized gradient approximation (GGA) with the Perdew, Burke, and Ernzerhof (PBE) functional [32,33]. Dudarev's approach for DFT+*U* calculations is used to correct for the inadequate description of localized 3d electrons on transition metals and 4f electrons on lanthanides [34]. A U-J parameter of 4.0 eV was chosen for the Fe 3d electrons where the selection of this value is based on a method validation study by Ota et al. for the $Sr_3Fe_2O_{7-\delta}$ system [15,26]. A U-J parameter of 6.0 eV was chosen for Pr 4f electrons based on earlier studies of PrO_2 [35,36]. The nuclei and core electrons were represented by the frozen-core projector-augmented wave (PAW) approach using the following valence configurations: Sr (4s4p5s), Pr (5p6s4f), Fe (3p3d4s), and O (2s2p) [37]. The plane-wave basis set was set to a kinetic cutoff of 750 eV. Integration over the Brillouin zone used the tetrahedron method with Blöchl corrections for all calculations [38]. All unit cell and 2 × 2 × 1 supercell calculations utilized a 9 × 9 × 3 and 5 × 5 × 3 Monkhorst-Pack (MP) k-point mesh, respectively [39]. The convergence criteria for SCF energy calculations and ionic relaxations were set to 10^{-6} eV and 0.02 eV/Å, respectively.

A 56 atom 2 × 2 × 1 supercell of SPF shown in Fig. S1a was utilized for the oxygen defect calculations. The dopant-configuration models were developed using the site-occupancy disorder (SOD) package on the 2 × 2 × 1 supercell of Sr_2FeO_4, that allowed us to compute all possible non-symmetrical dopant-configurations [40]. In order to minimize the computational complexity of this study, all structures generated by SOD were initially optimized with the same initial magnetic moment configuration, denoted as configuration A in Fig. S1b. The lowest energy structure identified for each dopant-configuration was selected as the representative model structure for further calculations. In order to identify the most stable magnetic configuration for iron, the representative model structure for each dopant configuration was then tested with different possible magnetic moment configurations presented in Fig. S1b. The formation of oxygen vacancy defects ($V_O^\times$ in Kröger-Vink notation [41]) was examined considering all non-identical oxygen atoms in the 56-atom supercell. The representative sites used for interstitial defect simulations ($O_i^\times$) are illustrated in Fig. S2.

Formation free energies of oxygen defects, in each charge state q, were calculated utilizing the following equation:

$$\Delta G_f(q) = E_{defect} - E_{pristine} \pm n_o(E_o + \mu_o) + q(E_{VBM} + E_F) + E_{corr} \quad (1)$$

where E_{defect} being the SCF energy of the relaxed supercell containing a defect in charge state q, $E_{pristine}$ being the SCF energy of the pristine supercell in a neutral charge state, n_o being the number of oxygen atoms removed or added to the pristine supercell, E_o and μ_o correspond to the energy and chemical potential of an oxygen atom, respectively (referenced to half the energy and chemical potential of a gas phase O_2 molecule). Based on the vibrational analysis of the pristine and vacancy structures of Sr_2FeO_4 that indicate these contributions cancel each other out (see Table S1), further vibrational contributions are not calculated for all other dopant-configurations [42,43]. The chemical

potential of an oxygen molecule, μ_{O2} (T, p°), is calculated using the following expression with reference to a total pressure p° of 1 atm:

$$\mu_{O2} = \mu_{O2}(T, p^\circ) + k_b T ln\left(\frac{p_{O2}}{p^\circ}\right) \quad (2)$$

It is well known that GGA tends to overestimate the binding energy of the O_2 molecule and therefore, we utilize the following correction scheme based on the H_2O splitting reaction to calculate E_{O2} [44–46]:

$$E_{O2}^{tot} = 2[(E_{H2O}^{DFT} + E_{H2O}^{ZPE}) - (E_{H2}^{DFT} + E_{H2}^{ZPE}) - E_{HOF}] - E_{O2}^{ZPE} \quad (3)$$

Here, E_i^{ZPE} is the experimental zero-point energy of the corresponding gas molecules, E_{HOF} is the experimental heat of formation of a gas-phase H_2O molecule (T=0 K), and E_i^{DFT} is the energy calculated with PBE functional. E_{VBM} in eqn. (1) is the energy of the valence band maximum (VBM) for the pristine supercell, and E_F is equal to the Fermi energy referenced with respect to the VBM. E_{corr} is calculated utilizing the python charged defect toolkit (pyCDT) [47]. pyCDT calculates two correction terms: the image-charge correction via the Kumagai and Oba scheme [48–50] and the potential alignment correction. The self-consistent Fermi energy is calculated using the SC-FERMI code [42,51]. For all oxygen migration calculations, we utilized the nudged elastic band (NEB) algorithm to determine the minimum energy pathway [52]. All spring forces were converged to 0.025 eV/Å. For Bader charge analysis, we utilized the Henkelman algorithm [52,53]. All structures are visualized with VESTA [54]. Lastly, we computed the phase stability of all considered dopant configurations at T = 0 K, i.e., we are neglecting entropy contributions. Details of these calculations are presented in section S1 of the Supplementary Information.

3. Results and Discussion

3.1 Structural and Electronic Properties

Utilizing the site-occupancy disorder (SOD) package, the 2 × 2 × 1 supercell of $(Sr_{1-x}Pr_x)_2FeO_4$ (x = 0) was converted into 7, 42, 122 and 181 possible non-symmetrical conformers for x = 0.125, 0.25, 0.375 and 0.5, respectively. In order to elaborate on the phase stability of each dopant-configuration (see section S1), we compute that Sr_2FeO_4 and $SrPrFeO_4$ are stable dopant-configurations. For $Sr_{1.75}Pr_{0.25}FeO_4$, $Sr_{1.5}Pr_{0.5}FeO_4$, and $Sr_{1.25}Pr_{0.75}FeO_4$, we compute 0.001163, 0.000405, and 0.000938 eV/atom above the convex hull, respectively, i.e., these structures are practically on the convex hull and thus, at least a large fraction of these structures is thermodynamically stable. The thermodynamic stability of $SrPrFeO_4$ is observed experimentally as a sintering co-product under hydrogen conditions for the RP $PrSrFe_{0.8}Ru_{0.1}Nb_{0.1}O_{4+\delta}$, and perovskites $Pr_{0.4}Sr_{0.6}(Co_{0.2}Fe_{0.8})_{1-x}Mo_xO_{3-\sigma}$ and $Pr_{0.42}Sr_{0.6}Co_{0.2}Fe_{0.7}Nb_{0.1}O_{3-\sigma}$ [55–57]. We present the calculated volumes of all supercell conformers and their relative energies in Fig. S3 and Tables S2-S5, respectively. The lowest energy configurations identified from this analysis are illustrated in Fig. 1 and these conformers were selected for further study. The configurational entropy that accompanies dopant-configurations with a greater degree of disorder is expected to decrease the relative free energy at high temperatures, a parameter that is ignored in this study to limit the computational effort. A clear observation upon Pr^{3+} introduction to Sr_2FeO_4 is the preferential formation of a clean SrO layer and a mixed Sr/PrO rocksalt layer segmented by the FeO_2 layers. For x = 0.5, the lowest energy structure has two distinct rocksalt layers composed of SrO and PrO as displayed in Fig. 1e. Table S6 outlines the relative energy distribution of each model dopant-configuration as a function of the initial iron magnetic moment configurations presented in Fig. S1b. For each dopant-configuration, we select the magnetic configuration with a relative minimum energy for further analysis. For undoped Sr_2FeO_4, our calculations predicted similar energies for FM and AFM configurations. However, electronic structure calculations revealed a metallic

behavior for the FM configurations (Fig. S4) and a small band gap was observed for AFM configurations as explained in the later section and Fig. 3a. Since experimental studies reported a band gap of 0.8 – 1.0 eV [58,59] for Sr_2FeO_4, we chose the AFM configuration for further analysis. Increasing the Pr^{3+} concentration increases the average magnetic moment of Fe as the number of high spin (HS) Fe^{4+} are reduced to HS Fe^{3+}. This relationship is consistent for all starting magnetic configurations indicating that the predicted oxidation state of Fe is independent of the starting magnetic configuration.

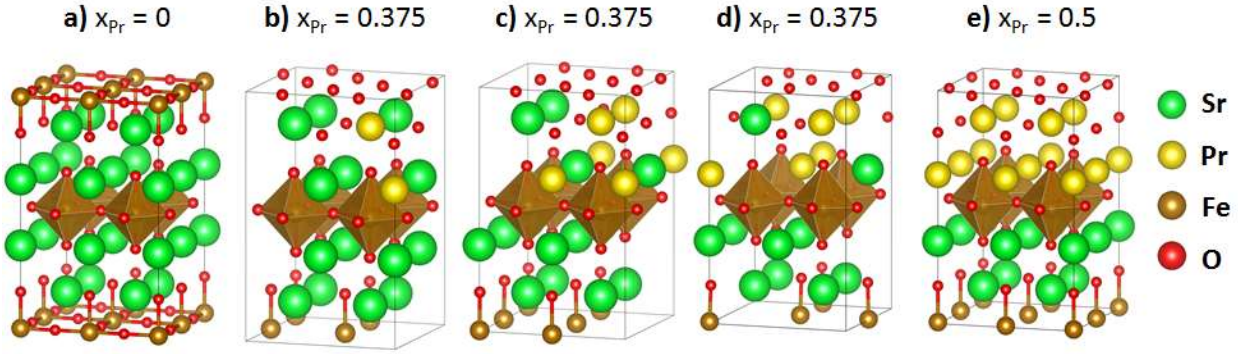

Fig. 1: Polyhedral representations of the lowest energy dopant-configurations for a) Sr_2FeO_4, b) $Sr_{1.75}Pr_{0.25}FeO_4$ (structure 7), c) $Sr_{1.5}Pr_{0.5}FeO_4$ (structure 23), d) $Sr_{1.25}Pr_{0.75}FeO_4$ (structure 56), and e) $SrPrFeO_4$ (structure 45).

Fig. 2 outlines the supercell structural parameters of $(Sr_{1-x}Pr_x)_2FeO_4$ as a function of Pr^{3+} concentration. A gradual increase in the Pr content results in an expansion of the SPF supercell volume, elongation of Fe-O bonds, and a gradual decrease in Fe-O-Fe angles. Octahedral tilt increases with increasing Pr^{3+} content due to the mixed presence of +2 and +3 A-site atoms in the rocksalt layers. The observed increase in unit cell volume while substituting Sr^{2+} with Pr^{3+}, an ion with a smaller native ionic radius (1.18 Å vs 0.99 Å) [60], appears to be counterintuitive. A similar counterintuitive observation was made by Ritzmann et. al. where the introduction of Sr^{2+} to the A-site of the orthorhombic perovskite $LaFeO_{3-\delta}$ decreased the supercell volume and Fe-O bond

lengths, whereas the Fe-O-Fe angles increased toward 180° [61]. This behavior was attributed to the formation of electron holes that shift the (Sr,La)FeO_3 series from an insulator to a p-type semiconductor [61]. In order to understand such electronic effects of Pr^{3+} substitution to the Sr_2FeO_4 perovskite in this study, we examined the partial density of states (PDOS) plots of each dopant-configuration as displayed in Fig. 3.

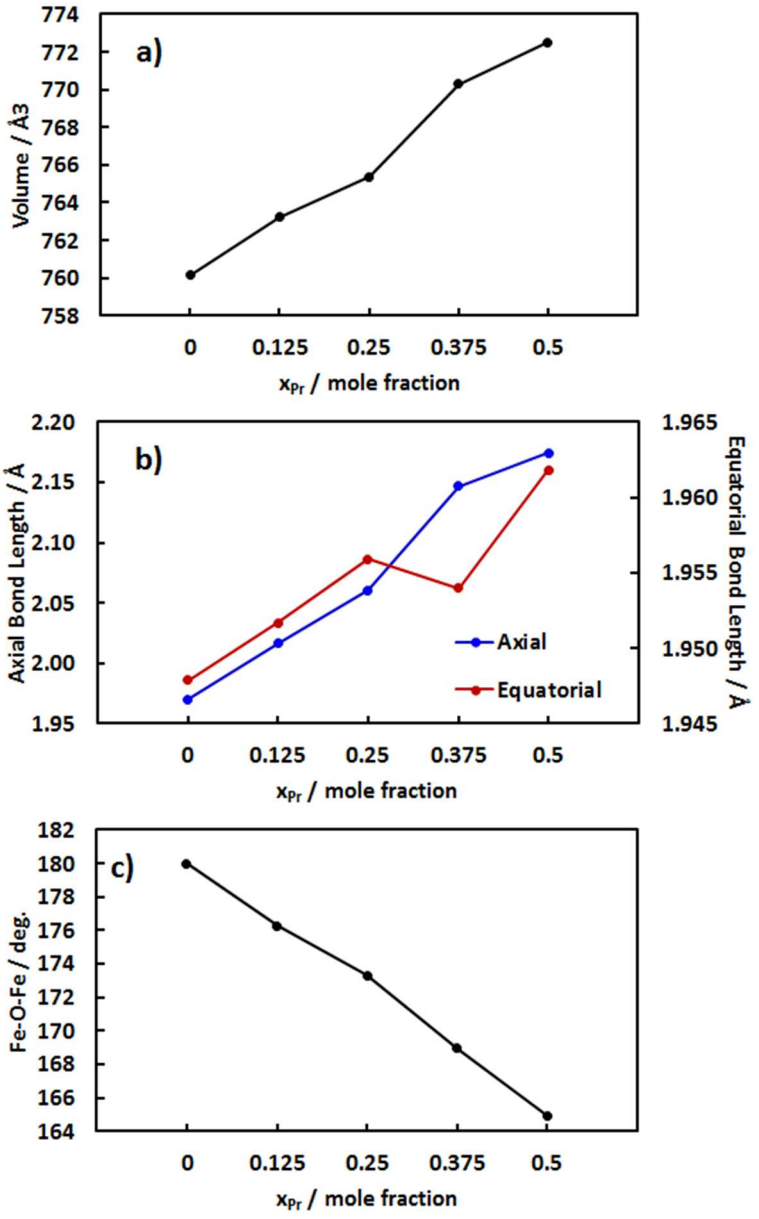

Fig. 2: Effect of Pr dopant concentration on the structural parameters of $(Sr_{1-x}Pr_x)_2FeO_4$ a) cell volume ($Å^3$), b) average Fe-O bond lengths (Å), and c) average Fe-O-Fe angle (deg.).

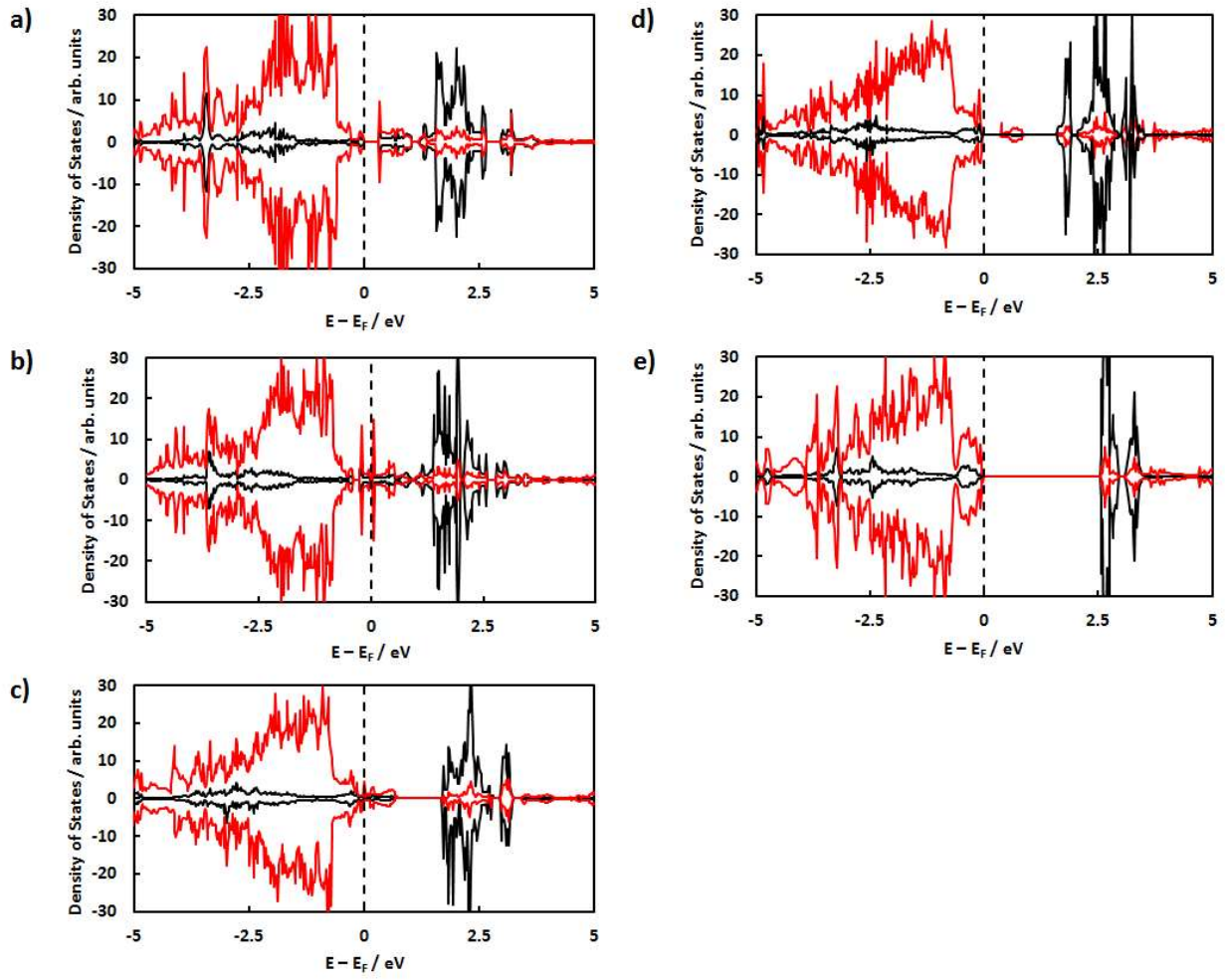

Fig. 3: PDOS for Fe 3d (black) and O 2p (red) states for $(Sr_{1-x}Pr_x)_2FeO_4$: a) x = 0, b) x = 0.125, c) x = 0.25, d) = 0.375, and e) x = 0.5. Energies are referred to the Fermi level (E_F). Positive PDOS values represent α-spins states and negative values represent β-spin states.

A small band gap of 0.34 eV was observed for Sr_2FeO_4 (Fig. 3a) which is smaller than the experimental value (0.8-1.0 eV [58,62]) due to the well-known error of GGA which tends to underestimate semiconductor bandgaps and overestimate computed unit cell lattice constants [63]. The electronic structure of the $(Sr_{1-x}Pr_x)_2FeO_4$ system exhibits a metallic character when x = 0.125 and 0.25, semiconductor behavior when x = 0.375, and an insulator behavior for x = 0.5. Noticeably for x = 0.375 (Fig. 3d), a small band of O 2p states appear in the band gap suggesting a semiconductor behavior, whereas a clear large gap of 2.55 eV was observed for x = 0.5 (Fig. 3e)

suggesting that the system became an insulator. To understand the significant increase in the width of the band gap from x = 0.375 and 0.5, we examined the effect of Pr^{3+}concentration on the oxidation state and magnetic moment of iron. As the content of Pr^{3+} increases, charge compensation is required to maintain system electroneutrality which can be achieved by changing the oxidation state of iron. Introduction of Pr^{3+} is expected to reduce the oxidation state of iron from 4+ (x = 0) to a mixture of 3+/4+ (x = 0.125 to 0.375) and to 3+ (x = 0.5). To establish the effects of charge compensation as the system is reduced, we analyze the magnetic moment of iron and the computed Bader charges for each element as shown in Table 1.

Table 1: Average Fe magnetic moment (μ_B) and Bader charges (e) for $(Sr_{1-x}Pr_x)_2FeO_{4\pm\delta}$ with and without oxygen vacancy ($V_O^{\times}$) and interstitial oxygen ($O_i^{\times}$) defects for x = 0, 0.125, 0.25, 0.375, and 0.5.

		x = 0	x = 0.125	x = 0.25	x = 0.375	x = 0.5
Pristine	μ_{Fe}	3.73	3.84	3.91	4.02	4.10
	q_{Fe}	1.73	1.74	1.73	1.74	1.75
	q_O	-1.21	-1.25	-1.27	-1.31	-1.35
	q_{Sr}	1.56	1.55	1.54	1.54	1.53
	q_{Pr}	---	2.11	2.10	2.10	2.12
With $V_O^{\times}$	μ_{Fe}	3.82	3.81	3.99	4.08	3.97
	q_{Fe}	1.72	1.72	1.70	1.70	1.59
	q_O	-1.24	-1.27	-1.31	-1.34	-1.34
	q_{Sr}	1.54	1.54	1.55	1.54	1.53
	q_{Pr}	---	2.08	2.09	2.09	2.08
With $O_i^{\times}$	μ_{Fe}	3.68	3.81	3.90	4.02	4.10
	q_{Fe}	1.79	1.81	1.76	1.70	1.72
	q_O	-1.19	-1.22	-1.24	-1.27	-1.30
	q_{Sr}	1.55	1.55	1.55	1.54	1.53
	q_{Pr}	---	2.11	2.10	2.11	2.11

In the case of pristine $(Sr_{1-x}Pr_x)_2FeO_4$, increasing the Pr^{3+} content increases the magnetic moment of iron. While the Bader charge of iron stays constant, the Bader charge of O becomes more negative. The increase in the magnetic moment of Fe is expected as the number of HS d^4 Fe^{4+} decreases with increasing Pr^{3+} content and the number of Fe^{3+} HS d^5 states increases, according to crystal field theory [64]. The invariance of the iron Bader charge is not unexpected and is explained in terms of the iron sublattice directly donating charge onto the oxygen sublattice upon reduction. Furthermore, the PDOS plots illustrated in Fig. 3 revealed that the magnitude of O 2p states below the Fermi level increases with Pr^{3+} introduction indicating an increased charge delocalization across the oxygen sublattice as opposed to charge localization across the iron sublattice. Therefore, increasing Pr^{3+} reduces the system which shifts the Fermi level up relative to the vacuum [65].

3.2 Oxygen Defect Formation

Here, we examine the stability of oxygen defects in SPF with respect to Pr^{3+} concentration. The formation energies of various oxygen vacancies ($V_O^{\times}$) and interstitial oxygen ($O_i^{\times}$) defects were calculated using Eq. (1). The configurations with lowest defect formation energy identified for each defect type with respect to Pr^{3+} concentration are illustrated in Fig. 4 and the corresponding defect formation energies are presented in Table 2. Magnetic moment variation tests for each minimum defect are presented in Table S7. These energies outline the following trends: the vacancy formation energy is essentially constant from x = 0 to 0.375 with a dramatic increase between x = 0.375 and 0.5, and interstitial formation energy decreases gradually with increasing Pr^{3+} concentration except for a slight negative deviation for x = 0.125. Free energies of these defect formations (ΔG) calculated at anodic (T=1073 K; $P_{O2}=10^{-20}$ atm) and cathodic (T=1073 K;

P_{O2}=0.21 atm) conditions suggest that the formation of vacancy defects is favorable compared to the interstitial oxygen defects at both anodic and cathodic conditions for x = 0 to 0.375. In the case of x = 0.5, formation of an interstitial oxygen defect is more favorable than the vacancy defect under cathodic conditions. The defect formation energies calculated for SPF seem to be lower than the vacancy formation energies reported for other n = 1 RP oxides. For example, the equatorial and apical vacancy formation energies for La-based cuprate (La_2CuO_4) were reported as 3.02 eV and 4.48 eV [66], respectively and that of La-based nickelate (La_2NiO_4) were 3.73 and 4.01 eV, respectively [67]. Sr-based manganate doped with Ce ($Ce_xSr_{2-x}MnO_4$) displayed a minimum vacancy formation energy of 1.76 eV [68] which is closer to the values calculated for SPF. These studies suggest that the vacancy defect formation is favored in A^{2+}-based RP oxides due to the more positive oxidation state of the B-site TM.

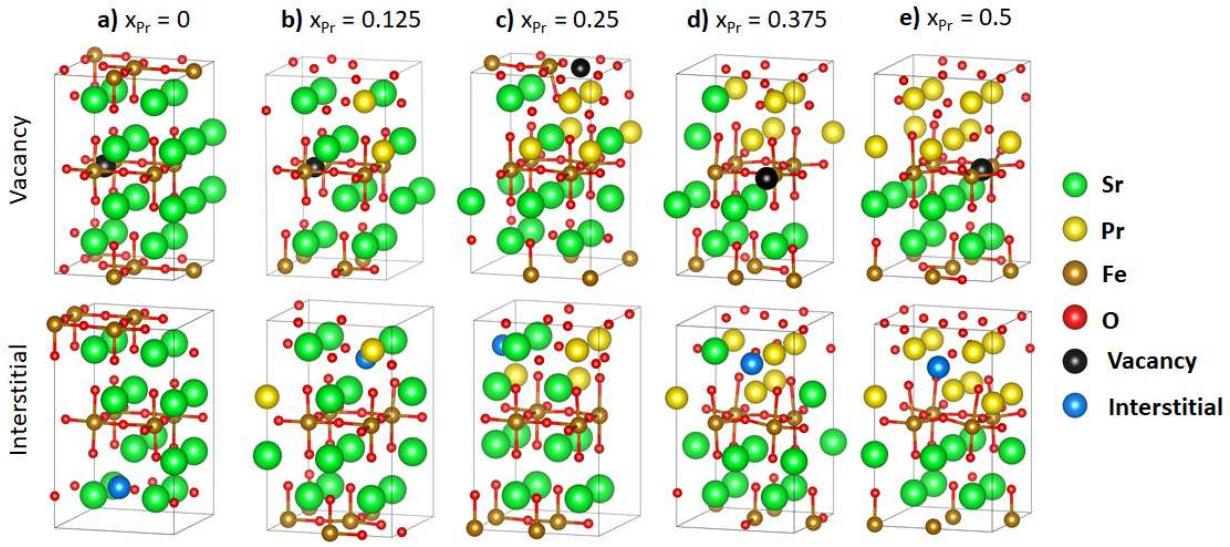

Fig. 4: Lowest energy oxide defect conformers identified for $(Sr_{1-x}Pr_x)_2FeO_{4\pm\delta}$ a) x = 0, b) x = 0.125, c) x = 0.25, d) x = 0.375, and e) x = 0.5. δ is modeled as a value of ±0.125.

Table 2: Formation energies (in eV) of oxygen vacancies ($\Delta E_{f,vac}$) and interstitial oxygen defects ($\Delta E_{f,int}$) calculated for $(Sr_{1-x}Pr_x)_2FeO_{4\pm\delta}$ with x = 0, 0.125, 0.25, 0.375, and 0.5. Free energies of these defect formation (ΔG) are calculated at anodic (T=1073 K; $P_{O2}=10^{-20}$ atm) and cathodic (T=1073 K; $P_{O2}=0.21$ atm) conditions. The reported numbers correspond to the structures presented in Fig. 4 and are calculated with a charge state of q = 0.

			1073 K, $P_{O2} = 10^{-20}$ atm		1073 K, $P_{O2} = 0.21$ atm	
x	**$\Delta E_{f,vac}$ (0 K)**	**$\Delta E_{f,int}$ (0 K)**	**$\Delta G_{f,vac}$**	**$\Delta G_{f,int}$**	**$\Delta G_{f,vac}$**	**$\Delta G_{f,int}$**
0	1.465	0.578	-1.910	3.953	0.198	1.845
0.125	1.497	0.294	-1.879	3.670	0.230	1.561
0.25	1.302	0.447	-2.074	3.822	0.035	1.714
0.375	1.617	0.283	-1.759	3.659	0.350	1.550
0.5	3.876	0.146	0.488	3.509	2.597	1.400

Table 3: Magnetic moment (μ_B) and Bader charges (e) of nearest neighbor(s) Fe to the oxide defect for $(Sr_{1-x}Pr_x)_2FeO_{4\pm\delta}$ with x = 0, 0.125, 0.25, 0.375, and 0.5.

	x = 0		x = 0.125		x = 0.25		x = 0.375		x = 0.5	
	Pristine	**With Defect**	**Pristine**	**With Defect**	**Pristine**	**With Defect**	**Pristine**	**With Defect**	**Pristine**	**With Defect**
Vacancy										
q_{Fe}	1.73, 1.73	1.75, 1.75	1.74, 1.74	1.72, 1.73	1.73, 1.71	1.66, 1.64	1.75, 1.73	1.64, 1.64	1.75, 1.75	1.21, 1.22
μ_{Fe}	3.73, 3.73	3.65, 3.65	3.85, 3.85	3.31, 3.31	3.81, 3.78	3.99, 4.03	4.07, 4.10	4.03, 4.02	4.10, 4.10	3.60, 3.60
Interstitial										
q_O^*	---	-0.69	---	-0.75	---	-0.75	---	-0.74	---	-0.76
q_{Fe}	1.73	1.84	1.74	1.80	1.73	1.75	1.74	1.62	1.75	1.72
μ_{Fe}	3.73	3.67	3.85	3.91	3.81	3.88	3.85	3.84	4.10	4.09

In order to explain the trends observed in vacancy defect formation of SPF, we examine how the average Bader charges of iron (Table 1) as well as the Bader charges on the nearest irons to the vacancy defect (Table 3) change as a function of Pr^{3+} concentration. As a vacancy is formed, the average iron Bader charge is essentially constant from x = 0 to x = 0.375 but decreases by 0.16 e for x = 0.5.

The Bader charges on the nearest irons to the vacancy defect are essentially unchanged for x = 0 and x = 0.125, decrease by ~ 0.1 e for x = 0.25 and 0.375, and decrease by ~ 0.5 e for x = 0.5. Ideally, all the Fe atoms in SPF with x = 0.5 should be in a Fe^{3+} state, and therefore, further reduction of iron results in mixed Fe^{3+} and Fe^{2+} states. Table 3 displays that the magnetic moment of iron atoms nearest to the vacancy site in case of x = 0.5 is reduced by 0.5 compared to the pristine system confirming the reduction of iron to the HS d^6 Fe^{2+} state [64]. In addition, the calculated Bader charges for this system reveal that the electrons released upon vacancy formation are transferred to the next-nearest irons of the oxide defect resulting in the generation of Fe^{2+} as opposed to charge donation to the oxygen sublattice that was observed with Pr^{3+} introduction. To visualize such charge compensation during vacancy formation, we employ the degree of delocalization factor (λ) outlined by Muñoz-García et al. [69,70]:

$$\lambda = \frac{(N-1)\left(< q_{O,nonstoichiomet} > - < q_{O,stoichiometric} >\right)}{< q_{O,stoichiometric} >} \quad (4)$$

In Eqn. 4, N refers to the number of oxygen ions in the pristine supercell and $< q_{O,\ nonstoichiometric} >$ and $< q_{O,\ stoichiometric} >$ refer to the average Bader charge on the oxygen sublattice in the defect and pristine supercells, respectively. Visualizing this metric in Fig. 5, we identify that the vacancy formation energy is strongly dependent on how well charge is redistributed to the oxygen sublattice. The overreduction of iron in the case of x = 0.5 is unfavorable as excess charge upon vacancy formation is not redistributed to the oxygen sublattice, but directly localizes on the neighboring irons causing an increase in ionicity on the iron sublattice. Therefore, we conclude that the formation of less stable Fe^{2+} ions upon vacancy formation in the case of x = 0.5 is primarily responsible for the precipitous change in vacancy formation energy.

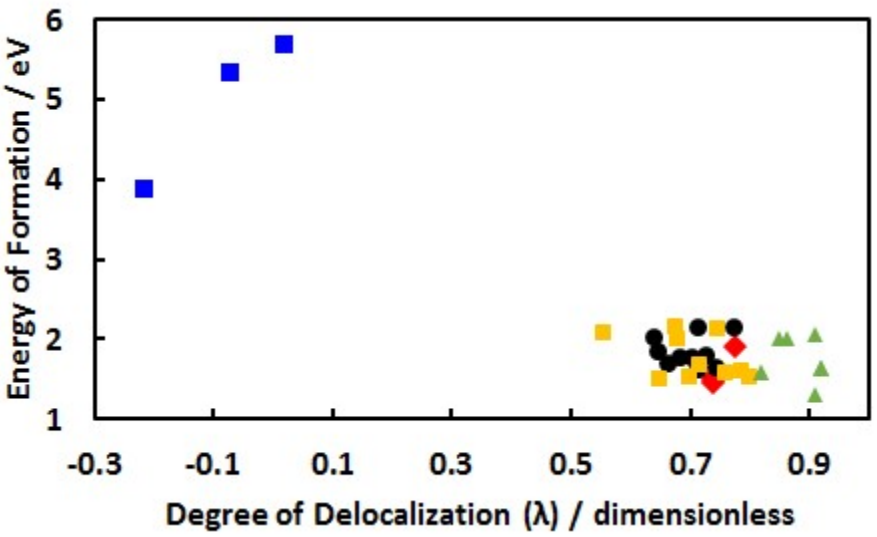

Fig. 5: The variation of $\Delta E_{f,vac}$ (in eV) with λ (dimensionless) for $Sr_2FeO_{4-\delta}$ (red), $Sr_{1.75}Pr_{0.25}FeO_{4-\delta}$ (yellow), $Sr_{1.5}Pr_{0.5}FeO_{4-\delta}$ (green), $Sr_{1.25}Pr_{0.75}FeO_{4-\delta}$ (black), and $SrPrFeO_{4-\delta}$ (blue).The lowest energy vacancy site and all non-equivalent sites are included in this figure. A positive λ value indicates an increase in the extent of charge that is absorbed into the oxygen sublattice.

The interstitial formation energy is found to decrease gradually as the Pr^{3+} concentration increases with a negative deviation observed for x = 0.125 (Table 2). While the vacancy defects are found to be most stable along the FeO_2 layer, interstitial defects are most stable in the rocksalt layers (e.g., SrO and PrO layers) as displayed in Fig. 4. The relationship among the average distance between the interstitial defect to its two neighboring A-site cations, A-site identity, and interstitial formation energy is illustrated in Fig. 6. The nearest neighbor elements to the interstitial oxygen were identified as (Sr, Sr) for x = 0 and x = 0.25, (Sr, Pr) for x = 0.125 and x = 0.375, and (Pr, Pr) for x = 0.5. For x = 0 and 0.25, which do not include a Pr^{3+} neighbor, the observed decrease in interstitial formation energy by 0.13 eV and a 0.554 Å decrease in the average A-site neighboring distance originate from the increased concentration of Pr^{3+} in the lattice. For all other configurations, the interstitial formation energy is determined directly by the preferential neighboring A-site configuration that maximizes the number of neighboring Pr^{3+} cations. Fig. 6

displays that the interstitial formation energy and average distance to its neighbors are very close for x = 0.125 and 0.375 with one Pr^{3+} neighbor. This also explains the negative deviation observed for x = 0.125 for which the interstitial oxygen formation is facilitated by the presence of neighboring Pr^{3+} cations compared to x = 0.25. A more favorable interstitial oxygen formation is observed for x = 0.5 which has two neighboring Pr^{3+} cations, although the average distance to its neighbors is very similar to those of x = 0.125 and 0.375. Therefore, the average distance of the interstitial defect to its nearest neighbors is a weak function of interstitial formation whereas the observed trend in interstitial formation energy is directly controlled by the identity of its neighboring A-site elements.

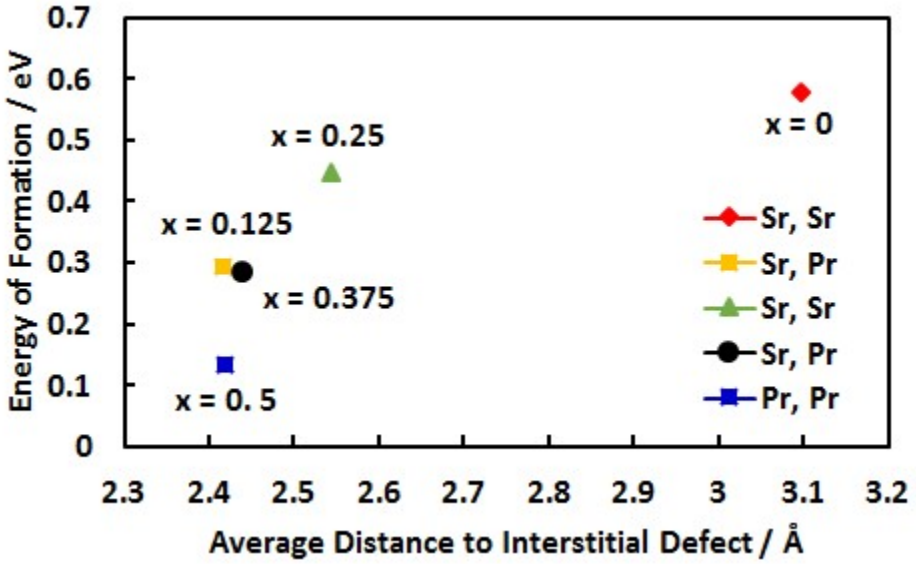

Fig. 6: Average distance of the minimum energy interstitial defect to neighboring A-site ions versus the energy of interstitial formation for x = 0 (red), x = 0.125 (yellow), 0.25 (green), 0.375 (black), and 0.5 (blue). The legend labels the elemental identity of the neighboring A-site ions.

Interstitial defects can be of two possible types: peroxide interstitial (O^{1-}) or oxide interstitial (O^{2-}). Table 3 outlines that the Bader charge of the interstitial defect for each dopant-configuration is ~ -0.75 e, a value that is ~ 55% of the average oxygen Bader charge. In all the minimum interstitial defect conformers displayed in Fig. 6, the interstitial oxygen binds to an axial oxygen.

The bond distances of these dimers (~ 1.5 Å, Table S8) are indicative of the formation of a peroxide interstitial defect as opposed to an oxide interstitial defect for which the O-O distance is expected to be ~ 2.6 Å [65,71]. Furthermore, the Bader charge on the next nearest oxygen atom to the defect is found to be very similar to that of the interstitial defect (Table S8). This result is consistent with the observation made by Xie et. al. that peroxide interstitials form via O^{2-} (lattice) + ½O_2 ⟶ O_2^{2-}, a reaction which does not involve redox chemistry in the system [65]. In addition, we found that the magnetic moment of iron is unaffected by the formation of an interstitial oxygen defect (Tables 1 and 3), i.e., we conclude that formation of an interstitial oxygen defect is not a redox process. As opposed to the vacancy formation energy, which is a strong function of charge compensation of the iron atoms neighboring the vacancy defect, the peroxide interstitial defect energy is primarily a function of the proximity of the peroxide defect to the neighboring cationic A-site.

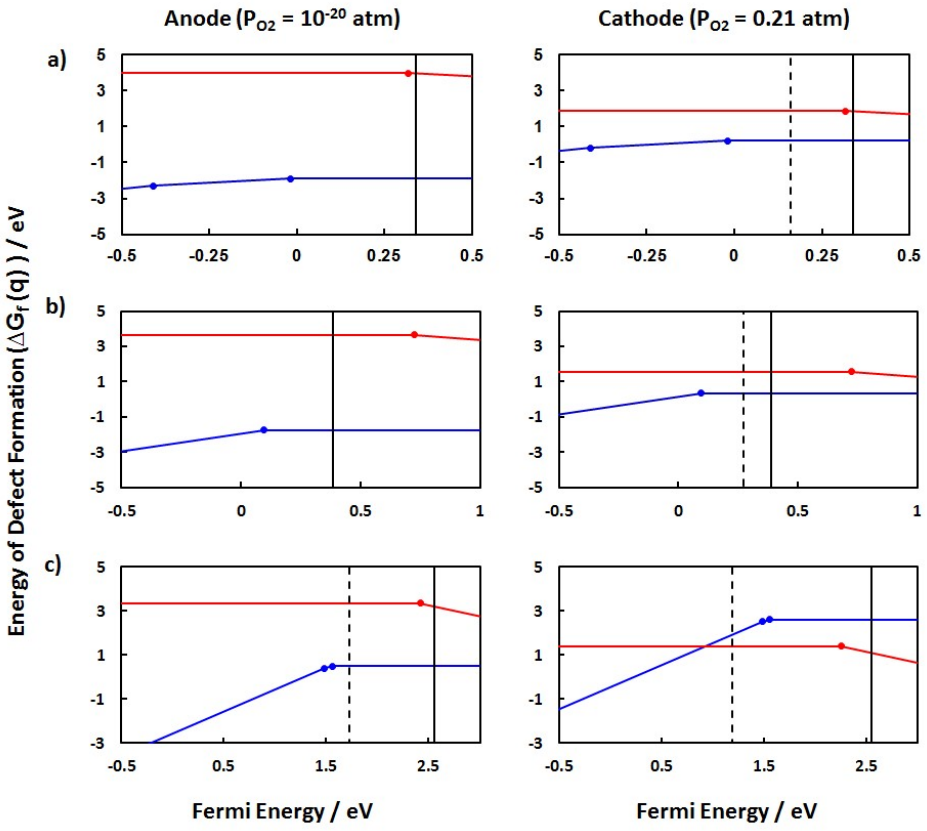

Fig. 7: Defect formation energy as a function of Fermi Energy at 800 °C for a) Sr_2FeO_4, b) $Sr_{1.25}Pr_{0.75}FeO_4$, and c) $SrPrFeO_4$. Configurations with x = 0.125 and x = 0.25 are not shown due to predicted metallic state. The blue and red lines represent the optimized vacancy and interstitial defect for each dopant-configuration, respectively. The dashed line represents the self-consistent Fermi-level, and the solid black lines represents the computed CBM for a given dopant-configuration.

The formation energies of charged defects for materials with a non-zero bandgap depend directly on the Fermi energy, E_F, as displayed in Eqn. 1. Therefore, we plot the formation energy of the relative lowest energy defect against the Fermi level for the following charge states: 2+, 1+, and 0 for the vacancy defect, and 1- and 0 for the peroxide interstitial defect. We also allow the external operating conditions to influence the defect formation energies by holding the temperature at 1073 K and partial pressure of oxygen at 10^{-20} atm and 0.21 atm corresponding to anodic and cathodic conditions, respectively [15,61]. To better interpret the electronic conduction behavior at

operating conditions, we compute the self-consistent Fermi level for each dopant-configuration [42,51]. The self-consistently computed Fermi level is unphysical for x = 0 and 0.375 dopant-configurations under anodic conditions. The prominence of highly negative vacancy formation energies for all values in the computed bandgap is a violation of the assumed non-interacting defect assumption at the dilute limit [51]. Despite the breakdown of the assumed non-interacting defect assumption, SPF appears to be of n-conductivity under anodic conditions due to a high concentration of electron releasing vacancy defects and a reduction of Fe^{4+} to Fe^{3+} upon vacancy formation [42]. Based on Fig. 7, we observe that the oxide vacancy is the dominant defect for dopant-configurations x = 0, 0.375, and 0.5 under anodic conditions. Charged defects are dominant for x = 0, 0.375, and 0.5 until a Fermi level of -0.019, 0.094, and 1.561 eV, respectively. Under cathodic conditions, the self-consistent Fermi level is always located within the band gap for each dopant-configuration and is located closer to the conduction band minimum (CBM) than the VBM for x = 0 and 0.375. Based on the self-consistent Fermi level, neutral oxygen vacancies are the dominant defects for x = 0 and 0.375. For x = 0.5, the neutral peroxide interstitial defect is the dominant oxide defect where the 2+ vacancy defect displays a 0.548 eV thermodynamic barrier at the computed self-consistent Fermi level, indicating that SPF under high Pr^{3+} concentration and atmospheric oxygen pressure is likely to exist in a slight hyperstoichiometric state, i.e., interstitials are more plentiful than vacancy defects.

3.3. Oxygen Migration

Bulk oxygen mobility is approximated by the self-diffusion coefficient, D_O (eqn. 5) [61,69].

$$D_O = C_{V_O^{\cdot\cdot}} D_V \tag{6}$$

The local vacancy defect concentration or $C_{V_O^{\cdot\cdot}}$ is determined by the vacancy formation free energy (ΔG_{vac}), and the vacancy diffusion coefficient or D_V (eqn. 5) is a function of the migration

free energy (ΔG_{mig}). The migration free energy is the energy required to migrate an oxide defect from one site to another [61]. Under the assumption of non-interacting vacancy defects, D_O can be expressed as following (eqn. 6).

$$D_O = Ae^{-(\Delta H_{f,vac}+\Delta H_{mig})/k_bT} \quad (6)$$

A or the preexponential factor incorporates the jump frequency of vacancy hopping and the entropy of vacancy formation and migration. The composite migration energy is the sum of the enthalpy of vacancy defect formation and the migration enthalpy. We approximate these enthalpies as the energy of vacancy formation and migration energy, respectively. We computed all non-equivalent jump routes of vacancy-mediated oxygen migration between the equilibrium defect site and next-nearest adjacent sites. Despite thermodynamic favorability under cathodic conditions, we did not compute the interstitial migration pathways for x = 0.5 and focused solely on the vacancy migration schemes for each dopant-configuration in order to determine trends in vacancy-mediated oxygen migration as a function of Pr^{3+} concentration. As depicted in Fig. 8, there are 3, 9, 9, 9, and 4 jump routes for the dopant-configurations with x = 0, 0.125, 0.25, 0.375, and 0.5, respectively. The relative energies of vacancy formation for all corresponding sites and the calculated barriers of migration are listed in Table 4.

Table 4 Migration energies (top number) and relative vacancy formation energies (bottom number in parenthesis) in eV for all non-identical oxygen vacancy migration jump routes. All relative energies (bottom number in parenthesis) are in reference to the minimum defect site (oxygen O1) for a given dopant-configuration that are illustrated in Figure 4.

	Dopant-Configuration				
Jump Route	**x = 0**	**X = 0.125**	**x = 0.25**	**x = 0.375**	**x = 0.5**
1. (O1 – O2)	2.652 (0.000)	3.638 (0.079)	3.892 (0.270)	3.539 (0.127)	5.710 (0.000)
2. (O1 – O3)	1.135 (0.000)	1.045 (0.031)	1.105 (0.319)	0.889 (0.127)	1.305 (0.000)
3. (O1 – O4)	1.009 (0.425)	1.027 (0.101)	1.132 (0.320)	0.947 (0.063)	2.813 (1.818)
4. (O1 – O5)	---	1.087 (0.021)	1.177 (0.319)	1.087 (0.175)	1.533 (1.461)
5. (O1 – O6)	---	0.869 (0.177)	1.130 (0.319)	1.058 (0.001)	---
6. (O1 – O7)	---	0.996 (0.640)	0.919 (0.699)	0.840 (0.384)	---
7. (O1 – O8)	---	0.985 (0.507)	1.084 (0.270)	1.104 (0.513)	---
8. (O1 – O9)	---	1.043 (0.574)	0.937 (0.698)	0.703 (0.204)	---
9. (O1 – O10)	---	1.062 (0.654)	1.152 (0.748)	1.039 (0.522)	---

Notably, path 1 for each dopant-configuration is highly unfavorable as migration barriers exceed 2.5 eV. Path 1 involves the longest oxide migration path that includes breaking the charge stabilization of the iron-oxygen sublattice in-the-FeO_2 plane. Introduction of Pr^{3+} slightly

decreases the in-the-FeO_2 plane migration barriers relative to Sr_2FeO_4 with x = 0.5 as an outlier. Compared to Sr_2FeO_4, the in-the-FeO_2 plane barriers remain unchanged for x = 0.25, decrease by ~ 0.1 to 0.3 eV for x = 0.125 and 0.375, and increase by ~ 0.2 eV for x = 0.5. Out-of-the-plane migration barriers directly depend on the local A-site ion composition above and below the FeO_2 plane. For migration into the pure SrO rocksalt layer, the migration barriers stay essentially constant for all configurations between x = 0 and 0.375 relative to Sr_2FeO_4 as the local A-site environment is similar. Energy barriers for migration into the mixed (Sr,Pr)O rocksalt layer decrease with increasing Pr^{3+} concentration with a maximum decrease of ~ 0.3 eV observed for x = 0.375 relative to Sr_2FeO_4. In both cases of in-the-plane and out-of-the-plane migration, decrease in migration barrier is observed with increased oxide defect proximity to Pr^{3+} which can be attested to a combined effect of Pr^{3+} having a greater ionic charge and smaller ionic radius than Sr^{2+}. The out-of-the-FeO_2 plane migration trend does not hold for x = 0.5 as vacancy formation in the pure SrO and PrO rocksalt layers are highly unfavorable relative to the minimum energy vacancy site. Therefore, the observed large increase in migration barrier for the out-of-the-FeO_2 plane migration in the case of x = 0.5 is possibly derived from a combined result of forming vacancy defects in rocksalt layers and the harsh charge localization penalty due to overreduction of iron as discussed in section 3.2. To compare vacancy-mediated migration to other n = 1 RP oxides, Routbort et. al. demonstrated experimentally for oxygen-deficient $La_{1.9}Sr_{0.1}CuO_{4-\delta}$ a barrier of 0.80 eV, a value lower than our SPF calculations [72]. As a comparison to $SrPrFeO_4$, a molecular dynamics study by Tealdi et. al. [73] displays for $LaSrCoO_{4-\delta}$ a barrier of 6.02 eV for in-the-plane migration path O1 – O2 (Table 4), a barrier range of 1.0 – 1.1 eV for in-the-plane migration path O1 – O3, and a barrier of 1.14 for out-of-the-plane migration path O1 – O5, values that are ~ 0.2 – 0.4 eV smaller than our calculation for $SrPrFeO_4$.

Next, we determine the favorable defect diffusion pathway based on the calculated composite oxide migration barriers for each dopant configuration (Table S9). The computed primary jump pathways are out-of-the-FeO_2 plane for x = 0.25 (path 5) and 0.375 (path 7); and in-the-FeO_2 plane for x = 0 (path 2), 0.125 (path 5), and 0.5 (path 2). As a first approximation to the self-diffusion coefficient under anodic and cathodic environmental conditions, we utilize ΔG_{vac} to determine the primary jump pathways under anodic and cathodic conditions. Under anodic conditions, the strongly negative free energy for x = 0 to 0.375 indicates that a high concentration of vacancy defects is thermodynamically strongly favorable (Table 2). For these negative energies, the primary jump pathways are determined solely by the migration energy for x = 0 to 0.375 with out-of-the-FeO_2 plane migration favored for x = 0 (path 3), 0.25 (path 6), and 0.375 (path 8); and in-the-FeO_2 plane migration for x = 0.125 (path 5) and 0.5 (path 2). Future work will investigate intermolecular defect corrections to the non-interacting defect assumption at the dilute limit. Under cathodic conditions, all free energies are above 0 eV; therefore, the primary jump pathways are out-of-the-FeO_2 plane for x = 0.25 (path 5) and 0.375 (path 7); and in-the-FeO_2 plane for x = 0 (path 2), 0.125 (path 5), and 0.5 (path 2). For x = 0.25, the thermodynamic barrier of 0.035 eV could require intermolecular defect corrections at the dilute limit.

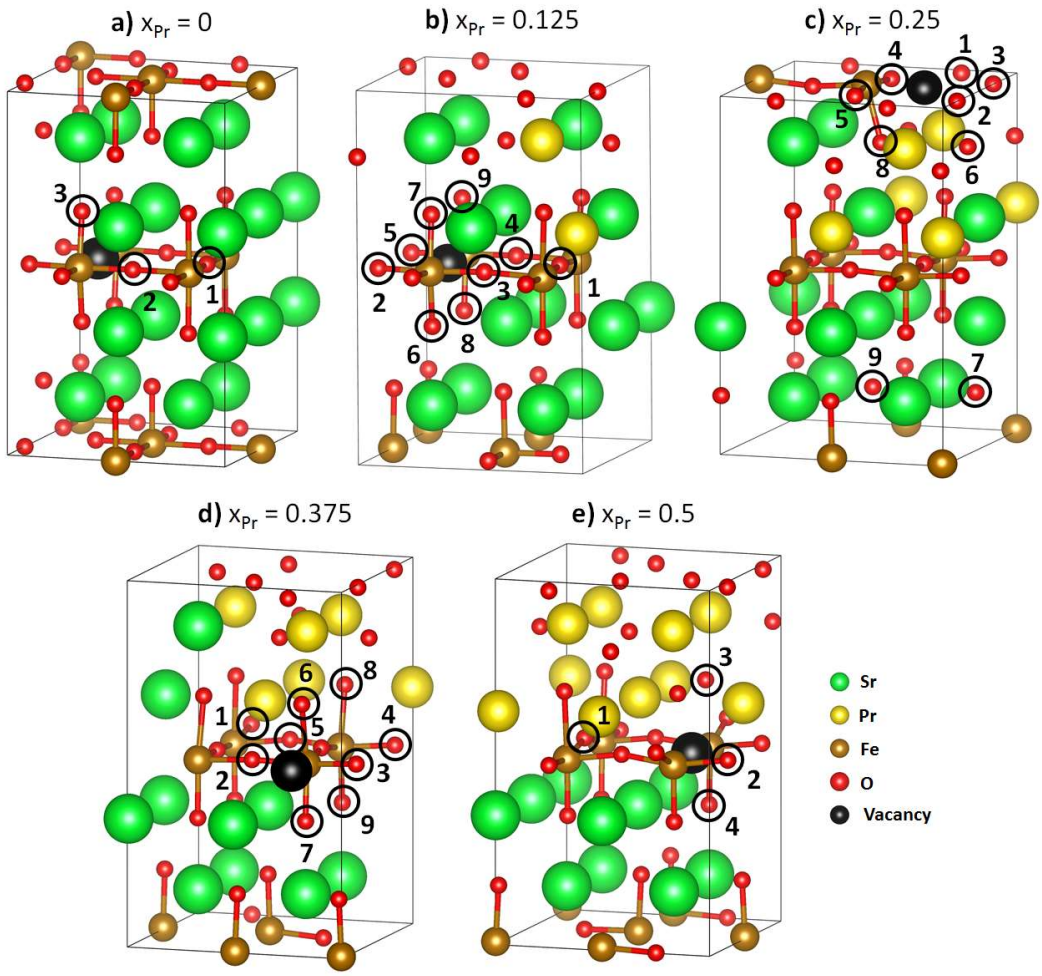

Fig. 8: Schematic of the vacancy migration jump routes around the minimum energy vacancy site (filled black circle) for a) Sr_2FeO_4, b) $Sr_{1.75}Pr_{0.25}FeO_4$, c) $Sr_{1.5}Pr_{0.5}FeO_4$, d) $Sr_{1.25}Pr_{0.75}FeO_4$, and e) $SrPrFeO_4$. The numbers presented inside the structures correspond to the jump routes presented in Table 4 for each dopant configuration.

4. Conclusions

We have presented a first principles DFT+U study displaying how Pr^{3+} substitution at the A-site influences oxygen defect formation and transport in $(Sr_{1-x}Pr_x)_2FeO_{4\pm\delta}$. A clear relationship between the structural and electronic properties of SPF are explained in terms of the average Fe oxidation state. Electronic conductivity improves with an introduction of small amounts (x = 0.125 and 0.25) of Pr^{3+} such that a mixture of Fe^{4+} and Fe^{3+} ions can coexist with an increased octahedral tilt to the lattice. The band gap increases and the system becomes an insulator when the Sr to Pr

ratio becomes 1:1. The vacancy formation energy remains nearly the same from x = 0 to x = 0.375 and a sharp increase is observed for x = 0.5 due to the overreduction of Fe. For dopant-configuration x = 0.5, all Fe atoms are already reduced to a 3+ oxidation state such that further reduction of Fe to a 2+ oxidation state upon vacancy formation becomes unfavorable. Interstitial defects exist in a peroxide state where the interstitial formation energy is directly related to the identity of the neighboring A-site element. The interstitial defect formation energy decreases with increasing proximity to Pr^{3+} as opposed to Sr^{2+}. Lastly, ionic conductivity is primarily controlled by a vacancy-mediated process due to the high concentration of vacancy defects under both anodic and cathodic conditions. Vacancy diffusion is especially costly for x = 0.5 due to the high energy of vacancy formation, especially in the rocksalt layer. Based on the interstitial favorability under cathodic conditions for x = 0.5, future work will investigate the role of interstitial-mediated diffusion for x = 0.5 and higher Pr^{3+} concentrations. Overall, introduction of small amounts of Pr^{3+} at the A-site improves the electronic conductivity of Sr_2FeO_4, and either improves or maintains a constant oxide diffusivity relative to Sr_2FeO_4. This study is intended to help the design and optimization of RP-based materials for direct use in SOFCs. Future studies will investigate the role of B-site variation with transitions metals like Co, Ni, and Cu as related to their effects on defect formation, redox stability, and oxide migration.

Acknowledgments

This work was sponsored by the National Science Foundation under Grant No. DMR- 1832809. In addition, this work was partially supported by the South Carolina Smart State Center for Strategic Approaches to the Generation of Electricity (SAGE). Computing resources provided by Extreme Science and Engineering Discovery Environment (XSEDE) facilities located at Texas

Advanced Computing Center (TACC) and San Diego Supercomputer Center (SDSC) (grand no. TG-CTS090100), U.S. Department of Energy facilities located at the National Energy Research Scientific Computing Center (NERSC) under Contract No. DE-AC02-05CH11231 and Pacific Northwest National Laboratory (Ringgold ID 130367, Grant Proposal 51711) and the High-Performance Computing clusters located at University of South Carolina are gratefully acknowledged.

Associated Content

Computational methodology for phase stability calculations. Vibrational contributions to free energy for Sr_2FeO_4. Relative energies and volumes of all possible conformers for each dopant-configuration. Relative energies of pristine and defect structures as a function of initial magnetic moment configurations. Bader charges and bond lengths for peroxide interstitial defects. Composite migration energy. 2 × 2 × 1 Sr_2FeO_4 model structure and all unique Fe magnetic moment arrangements. FM PDOS for Sr_2FeO_4. Interstitial sites tested for each dopant-configuration. This material is available free of charge via the Internet at http://pubs.acs.org.

Author Information

Corresponding Author

*Email: heyden@cec.sc.edu

Author Contributions

All authors have given approval to the final version of the manuscript.

Notes

The authors declare no competing financial interest.

References

(1) Sunarso, J.; Baumann, S.; Serra, J. M.; Meulenberg, W. A.; Liu, S.; Lin, Y. S.; Diniz da Costa, J. C. Mixed Ionic-Electronic Conducting (MIEC) Ceramic-Based Membranes for Oxygen Separation. *J. Memb. Sci.* **2008**, *320* (1–2), 13–41. https://doi.org/10.1016/j.memsci.2008.03.074.

(2) Zhang, C.; Sunarso, J.; Liu, S. Designing CO2-Resistant Oxygen-Selective Mixed Ionic–Electronic Conducting Membranes: Guidelines, Recent Advances, and Forward Directions. *Chem. Soc. Rev.* **2017**, *46* (10), 2941–3005. https://doi.org/10.1039/c6cs00841k.

(3) Riess, I. Mixed Ionic–Electronic Conductors—Material Properties and Applications. *Solid State Ionics* **2003**, *157* (1–4), 1–17. https://doi.org/10.1016/S0167-2738(02)00182-0.

(4) Adler, S. B. Factors Governing Oxygen Reduction in Solid Oxide Fuel Cell Cathodes. *Chem. Rev.* **2004**, *104* (10), 4791–4843. https://doi.org/10.1021/cr020724o.

(5) Yang, L.; Wang, S.; Blinn, K.; Liu, M.; Liu, Z.; Cheng, Z.; Liu, M. Enhanced Sulfur and Coking Tolerance of a Mixed Ion Conductor for SOFCs: BaZr0.1Ce0.7Y0.2–XYbxO3–δ. *Science (80-.).* **2009**, *326* (5949), 126–129. https://doi.org/10.1126/science.1174811.

(6) Gao, Z.; Mogni, L. V.; Miller, E. C.; Railsback, J. G.; Barnett, S. A. A Perspective on Low-Temperature Solid Oxide Fuel Cells. *Energy Environ. Sci.* **2016**, *9* (5), 1602–1644. https://doi.org/10.1039/c5ee03858h.

(7) Brett, D. J. L.; Atkinson, A.; Brandon, N. P.; Skinner, S. J. Intermediate Temperature Solid Oxide Fuel Cells. *Chem. Soc. Rev.* **2008**, *37* (8), 1568–1578. https://doi.org/10.1039/b612060c.

(8) Steele, B. C. H.; Heinzel, A. Materials for Fuel-Cell Technologies. *Nature*. 2001, pp 345–352. https://doi.org/10.1038/35104620.

(9) Shao, Z.; Haile, S. M. A High-Performance Cathode for the next Generation of Solid-Oxide Fuel Cells. *Nature* **2004**, *3* (1978), 170–173. https://doi.org/https://doi.org/10.1038/nature02863.

(10) Tietz, F.; Haanappel, V. A. C.; Mai, A.; Mertens, J.; Stöver, D. Performance of LSCF Cathodes in Cell Tests. *J. Power Sources* **2006**, *156* (1 SPEC. ISS.), 20–22. https://doi.org/10.1016/j.jpowsour.2005.08.015.

(11) Fu, C.; Sun, K.; Zhang, N.; Chen, X.; Zhou, D. Electrochemical Characteristics of LSCF–SDC Composite Cathode for Intermediate Temperature SOFC. *Electrochim. Acta* **2007**, *52* (13), 4589–4594. https://doi.org/10.1016/j.electacta.2007.01.001.

(12) Yang, C.; Yang, Z.; Jin, C.; Xiao, G.; Chen, F.; Han, M. Sulfur-Tolerant Redox-Reversible Anode Material for Direct Hydrocarbon Solid Oxide Fuel Cells. *Adv. Mater.* **2012**, *24* (11), 1439–1443. https://doi.org/10.1002/adma.201104852.

(13) Liu, Q.; Dong, X.; Xiao, G.; Zhao, F.; Chen, F. A Novel Electrode Material for Symmetrical SOFCs. *Adv. Mater.* **2010**, *22* (48), 5478–5482. https://doi.org/10.1002/adma.201001044.

(14) Xiao, G.; Liu, Q.; Zhao, F.; Zhang, L.; Xia, C.; Chen, F. Sr2Fe1.5Mo0.5O6 as Cathodes for Intermediate-Temperature Solid Oxide Fuel Cells with La0.8Sr0.2Ga0.87Mg0.13O3 Electrolyte. *J. Electrochem. Soc.* **2011**, *158* (5). https://doi.org/10.1149/1.3556085.

(15) Suthirakun, S.; Ammal, S. C.; Muñoz-García, A. B.; Xiao, G.; Chen, F.; Zur Loye, H. C.; Carter, E. A.; Heyden, A. Theoretical Investigation of H2 Oxidation on the Sr2Fe1.5Mo0.5O6 (001) Perovskite Surface under Anodic Solid Oxide Fuel Cell Conditions. *J. Am. Chem. Soc.* **2014**, *136* (23), 8374–8386. https://doi.org/10.1021/ja502629j.

(16) Jiang, Y.; Wang, S.; Zhang, Y.; Yan, J.; Li, W. Kinetic Study of the Formation of Oxygen Vacancy on Lanthanum Manganite Electrodes. *J. Electrochem. Soc.* **1998**, *145* (2), 373–378. https://doi.org/10.1149/1.1838271.

(17) Jiang, S. P. Development of Lanthanum Strontium Cobalt Ferrite Perovskite Electrodes of Solid Oxide Fuel Cells – A Review. *Int. J. Hydrogen Energy* **2019**, *44* (14), 7448–7493. https://doi.org/10.1016/j.ijhydene.2019.01.212.

(18) Švarcová, S.; Wiik, K.; Tolchard, J.; Bouwmeester, H. J. M.; Grande, T. Structural Instability of Cubic Perovskite BaxSr1 - XCo1 - YFeyO3 - δ. *Solid State Ionics* **2008**, *178* (35–36), 1787–1791. https://doi.org/10.1016/j.ssi.2007.11.031.

(19) Hernández, A. M.; Mogni, L.; Caneiro, A. La2NiO4+δ as Cathode for SOFC: Reactivity Study with YSZ and CGO Electrolytes. *Int. J. Hydrogen Energy* **2010**, *35* (11), 6031–6036. https://doi.org/10.1016/j.ijhydene.2009.12.077.

(20) Guan, B.; Li, W.; Zhang, H.; Liu, X. Oxygen Reduction Reaction Kinetics in Sr-Doped La2NiO4+δ Ruddlesden-Popper Phase as Cathode for Solid Oxide Fuel Cells. *J. Electrochem. Soc.* **2015**, *162* (7), F707–F712. https://doi.org/10.1149/2.0541507jes.

(21) Chung, Y. S.; Kim, T.; Shin, T. H.; Yoon, H.; Park, S.; Sammes, N. M.; Kim, W. B.; Chung, J. S. In Situ Preparation of a La1.2Sr0.8Mn0.4Fe0.6O4 Ruddlesden–Popper Phase with Exsolved Fe Nanoparticles as an Anode for SOFCs. *J. Mater. Chem. A* **2017**, *5* (14), 6437–6446. https://doi.org/10.1039/c6ta09692a.

(22) Yang, C.; Li, J.; Lin, Y.; Liu, J.; Chen, F.; Liu, M. In Situ Fabrication of CoFe Alloy Nanoparticles Structured (Pr0.4Sr0.6)3(Fe0.85Nb0.15)2O7 Ceramic Anode for Direct Hydrocarbon Solid Oxide Fuel Cells. *Nano Energy* **2015**, *11*, 704–710. https://doi.org/10.1016/j.nanoen.2014.12.001.

(23) Huan, D.; Wang, Z.; Wang, Z.; Peng, R.; Xia, C.; Lu, Y. High-Performanced Cathode with a Two-Layered R–P Structure for Intermediate Temperature Solid Oxide Fuel Cells. *ACS Appl. Mater. Interfaces* **2016**, *8* (7), 4592–4599. https://doi.org/10.1021/acsami.5b10844.

(24) Kagomiya, I.; Jimbo, K.; Kakimoto, K. I.; Nakayama, M.; Masson, O. Oxygen Vacancy Formation and the Ion Migration Mechanism in Layered Perovskite (Sr,La)3Fe2O7−δ. *Phys. Chem. Chem. Phys.* **2014**, *16* (22), 10875–10882. https://doi.org/10.1039/c4cp00736k.

(25) Ling, Y.; Guo, T.; Zhang, X.; Budiman, R. A.; Fujimaki, Y.; Nakamura, T.; Lin, B.;

Kawada, T.; Amezawa, K. Evaluation of Electrical Conductivity and Oxygen Diffusivity of the Typical Ruddlesden-Popper Oxide Sr3Fe2O7-δ. *Ceram. Int.* **2017**, *43* (18), 16264–16269. https://doi.org/10.1016/j.ceramint.2017.08.211.

(26) Ota, T.; Kizaki, H.; Morikawa, Y. Mechanistic Analysis of Oxygen Vacancy Formation and Ionic Transport in Sr3Fe2O7−δ. *J. Phys. Chem. C* **2018**, *122* (8), 4172–4181. https://doi.org/10.1021/acs.jpcc.7b11904.

(27) Tan, W.; Huan, D.; Yang, W.; Shi, N.; Wang, W.; Peng, R.; Wu, X.; Lu, Y. A First-Principles Study on Divergent Reactions of Using a Sr3Fe2O7 Cathode in Both Oxygen Ion Conducting and Proton Conducting Solid Oxide Fuel Cells. *RSC Adv.* **2018**, *8* (47), 26448–26460. https://doi.org/10.1039/c8ra04059a.

(28) Fossdal, A.; Einarsrud, M. A.; Grande, T. Phase Equilibria in the Pseudo-Binary System SrO–Fe2O3. *J. Solid State Chem.* **2004**, *177* (8), 2933–2942. https://doi.org/10.1016/j.jssc.2004.05.007.

(29) Yang, C.; Yang, Z.; Jin, C.; Liu, M.; Chen, F. High Performance Solid Oxide Electrolysis Cells Using Pr0.8Sr1.2(Co,Fe)0.8Nb0.2O4+δ–Co–Fe Alloy Hydrogen Electrodes. *Int. J. Hydrogen Energy* **2013**, *38* (26), 11202–11208. https://doi.org/10.1016/j.ijhydene.2013.06.086.

(30) Tan, T.; Qin, M.; Li, K.; Zhou, M.; Liu, T.; Yang, C.; Liu, M. In-Situ Exsolved NiFe Alloy Nanoparticles on Pr0.8Sr1.2(NiFe)O4-δ for Direct Hydrocarbon Fuel Solid Oxide Fuel Cells. *Int. J. Hydrogen Energy* **2020**, *45* (53), 29407–29416. https://doi.org/10.1016/j.ijhydene.2020.07.250.

(31) Kresse, G.; Furthmüller, J. Efficient Iterative Schemes for Ab Initio Total-Energy Calculations Using a Plane-Wave Basis Set. *Phys. Rev. B - Condens. Matter Mater. Phys.* **1996**, *54* (16), 11169–11186. https://doi.org/10.1103/PhysRevB.54.11169.

(32) Perdew, J. P.; Wang, Y. Accurate and Simple Analytic Representation of the Electron-Gas Correlation Energy. *Phys. Rev. B* **1992**, *45* (7), 13244–13249. https://doi.org/10.1103/PhysRevB.98.079904.

(33) Perdew, J. P.; Yue, W. Accurate and Simple Density Functional for the Electronic Exchange Energy: Generalized Gradient Approximation. *Phys. Rev. B* **1986**, *33* (12), 8800–8802. https://doi.org/10.1103/PhysRevB.33.8800.

(34) Dudarev, S.; Botton, G. Electron-Energy-Loss Spectra and the Structural Stability of Nickel Oxide: An LSDA+U Study. *Phys. Rev. B - Condens. Matter Mater. Phys.* **1998**, *57* (3), 1505–1509. https://doi.org/10.1103/PhysRevB.57.1505.

(35) Zhou, F.; Ozoliņš, V. Obtaining Correct Orbital Ground States in F-Electron Systems Using a Nonspherical Self-Interaction-Corrected LDA+U Method. *Phys. Rev. B - Condens. Matter Mater. Phys.* **2009**, *80* (12), 1–6. https://doi.org/10.1103/PhysRevB.80.125127.

(36) Tran, F.; Schweifer, J.; Blaha, P.; Schwarz, K.; Novák, P. PBE+U Calculations of the Jahn-Teller Effect in PrO2. *Phys. Rev. B - Condens. Matter Mater. Phys.* **2008**, *77* (8), 1–9. https://doi.org/10.1103/PhysRevB.77.085123.

(37) Blöchl, P. E. Projector Augmented-Wave Method. *Phys. Rev. B* **1994**, *50* (24), 17953–17979. https://doi.org/10.1103/PhysRevB.50.17953.

(38) Blöchl, P. E.; Jepsen, O.; Andersen, O. K. Improved Tetrahedron Method for Brillouin-Zone Integrations. *Phys. Rev. B* **1994**, *49* (23), 16223–16233. https://doi.org/doi.org/10.1103/PhysRevB.49.16223.

(39) Pack, J. D.; Monkhorst, H. J. Special Points for Brillouin-Zone Integrations. *Phys. Rev. B* **1977**, *16* (4), 1748–1749. https://doi.org/10.1103/PhysRevB.16.1748.

(40) Grau-Crespo, R.; Hamad, S.; Catlow, C. R. A.; De Leeuw, N. H. Symmetry-Adapted Configurational Modelling of Fractional Site Occupancy in Solids. *J. Phys. Condens. Matter* **2007**, *19* (25). https://doi.org/10.1088/0953-8984/19/25/256201.

(41) Kröger, F. A.; Vink, H. J. Relations between the Concentrations of Imperfections in Solids. *J. Phys. Chem. Solids* **1958**, *5* (3), 208–223. https://doi.org/10.1016/0022-3697(58)90069-6.

(42) Taylor, F. H.; Buckeridge, J.; Catlow, C. R. A. Defects and Oxide Ion Migration in the Solid Oxide Fuel Cell Cathode Material LaFeO3. *Chem. Mater.* **2016**, *28* (22), 8210–8220. https://doi.org/10.1021/acs.chemmater.6b03048.

(43) Suthirakun, S.; Xiao, G.; Ammal, S. C.; Chen, F.; Zur Loye, H. C.; Heyden, A. Rational Design of Mixed Ionic and Electronic Conducting Perovskite Oxides for Solid Oxide Fuel Cell Anode Materials: A Case Study for Doped SrTiO3. *J. Power Sources* **2014**, *245*, 875–885. https://doi.org/10.1016/j.jpowsour.2013.07.040.

(44) Ammal, S. C.; Heyden, A. Modeling the Noble Metal/TiO2 (110) Interface with Hybrid DFT Functionals: A Periodic Electrostatic Embedded Cluster Model Study. *J. Chem. Phys.* **2010**, *133* (16). https://doi.org/10.1063/1.3497037.

(45) Nørskov, J. K.; Rossmeisl, J.; Logadottir, A.; Lindqvist, L.; Kitchin, J. R.; Bligaard, T.; Jónsson, H. Origin of the Overpotential for Oxygen Reduction at a Fuel-Cell Cathode. *J. Phys. Chem. B* **2004**, *108* (46), 17886–17892. https://doi.org/10.1021/jp047349j.

(46) Atkins, P.; Paula, J. De; Keeler, J. *Atkins' Physical Chemistry*, 11e ed.; Oxford University Press: Oxford, England, 2018.

(47) Broberg, D.; Medasani, B.; Zimmermann, N. E. R.; Yu, G.; Canning, A.; Haranczyk, M.; Asta, M.; Hautier, G. PyCDT: A Python Toolkit for Modeling Point Defects in Semiconductors and Insulators. *Comput. Phys. Commun.* **2018**, *226*, 165–179. https://doi.org/10.1016/j.cpc.2018.01.004.

(48) Freysoldt, C.; Neugebauer, J.; Van De Walle, C. G. Fully Ab Initio Finite-Size Corrections for Charged-Defect Supercell Calculations. *Phys. Rev. Lett.* **2009**, *102* (1), 1–4. https://doi.org/10.1103/PhysRevLett.102.016402.

(49) Freysoldt, C.; Neugebauer, J.; Van de Walle, C. G. Electrostatic Interactions between Charged Defects in Supercells. *Phys. Status Solidi Basic Res.* **2011**, *248* (5), 1067–1076. https://doi.org/10.1002/pssb.201046289.

(50) Kumagai, Y.; Oba, F. Electrostatics-Based Finite-Size Corrections for First-Principles

Point Defect Calculations. *Phys. Rev. B - Condens. Matter Mater. Phys.* **2014**, *89* (19). https://doi.org/10.1103/PhysRevB.89.195205.

(51) Buckeridge, J. Equilibrium Point Defect and Charge Carrier Concentrations in a Material Determined through Calculation of the Self-Consistent Fermi Energy. *Comput. Phys. Commun.* **2019**, *244*, 329–342. https://doi.org/10.1016/j.cpc.2019.06.017.

(52) Henkelman, G.; Arnaldsson, A.; Jónsson, H. A Fast and Robust Algorithm for Bader Decomposition of Charge Density. *Comput. Mater. Sci.* **2006**, *36* (3), 354–360. https://doi.org/10.1016/j.commatsci.2005.04.010.

(53) Tang, W.; Sanville, E.; Henkelman, G. A Grid-Based Bader Analysis Algorithm without Lattice Bias. *J. Phys. Condens. Matter* **2009**, *21* (8). https://doi.org/10.1088/0953-8984/21/8/084204.

(54) Momma, K.; Izumi, F. VESTA 3 for Three-Dimensional Visualization of Crystal, Volumetric and Morphology Data. *J. Appl. Crystallogr.* **2011**, *44* (6), 1272–1276. https://doi.org/10.1107/S0021889811038970.

(55) Qin, M.; Xiao, Y.; Yang, H.; Tan, T.; Wang, Z.; Fan, X.; Yang, C. Ru/Nb Co-Doped Perovskite Anode: Achieving Good Coking Resistance in Hydrocarbon Fuels via Core-Shell Nanocatalysts Exsolution. *Appl. Catal. B Environ.* **2021**, *299* (July), 120613. https://doi.org/10.1016/j.apcatb.2021.120613.

(56) Zhang, P.; Guan, G.; Khaerudini, D. S.; Hao, X.; Xue, C.; Han, M.; Kasai, Y.; Abudula, A. B-Site Mo-Doped Perovskite Pr0.4Sr0.6 (Co0.2Fe0.8)1-XMoxO3-σ (x = 0, 0.05, 0.1 and 0.2) as Electrode for Symmetrical Solid Oxide Fuel Cell. *J. Power Sources* **2015**, *276*, 347–356. https://doi.org/10.1016/j.jpowsour.2014.11.141.

(57) Zhang, P.; Guan, G.; Khaerudini, D. S.; Hao, X.; Xue, C.; Han, M.; Kasai, Y.; Abudula, A. Mechanisms of Methane Decomposition and Carbon Species Oxidation on the Pr0.42Sr0.6Co0.2Fe0.7Nb0.1O3-σ Electrode with High Catalytic Activity. *J. Mater. Chem. A* **2015**, *3* (45), 22816–22823. https://doi.org/10.1039/c5ta07599h.

(58) Chen, Y.; Jung, W.; Cai, Z.; Kim, J. J.; Tuller, H. L.; Yildiz, B. Impact of Sr Segregation on the Electronic Structure and Oxygen Reduction Activity of SrTi1-XFexO3 Surfaces. *Energy Environ. Sci.* **2012**, *5* (7), 7979–7988. https://doi.org/10.1039/c2ee21463f.

(59) Matsuno, J.; Okimoto, Y.; Kawasaki, M.; Tokura, Y. Variation of the Electronic Structure in Systematically Synthesized Sr2MO4 (M=Ti, V, Cr, Mn, and Co). *Phys. Rev. Lett.* **2005**, *95* (17), 1–4. https://doi.org/10.1103/PhysRevLett.95.176404.

(60) Shannon, R. D. Revised Effective Ionic Radii and Systematic Studies of Interatomie Distances in Halides and Chaleogenides. *Acta Crystallogr. Sect. A* **1976**, *32* (5), 751–767. https://doi.org/https://doi.org/10.1107/S0567739476001551.

(61) Ritzmann, A. M.; Muñoz-García, A. B.; Pavone, M.; Keith, J. A.; Carter, E. A. Ab Initio DFT+U Analysis of Oxygen Vacancy Formation and Migration in La1-XSrxFeO3-δ (x = 0, 0.25, 0.50). *Chem. Mater.* **2013**, *25* (15), 3011–3019. https://doi.org/10.1021/cm401052w.

(62) Adler, P.; Goncharov, A. F.; Syassen, K.; Schönherr, E. Optical Reflectivity and Raman

Spectra of Sr2FeO4 under Pressure. *Phys. Rev. B* **1994**, *50* (16), 11396–11402. https://doi.org/10.1103/PhysRevB.50.11396.

(63) He, L.; Liu, F.; Hautier, G.; Oliveira, M. J. T.; Marques, M. A. L.; Vila, F. D.; Rehr, J. J.; Rignanese, G. M.; Zhou, A. Accuracy of Generalized Gradient Approximation Functionals for Density-Functional Perturbation Theory Calculations. *Phys. Rev. B - Condens. Matter Mater. Phys.* **2014**, *89* (6), 1–15. https://doi.org/10.1103/PhysRevB.89.064305.

(64) Miessler, G. L.; Tarr, D. A. *Inorganic Chemistry*, 2nd ed.; Pearson Education, Inc. Pearson Prentice Hall: Upper Saddle River, New Jersey, 1998.

(65) Xie, W.; Lee, Y. L.; Shao-Horn, Y.; Morgan, D. Oxygen Point Defect Chemistry in Ruddlesden–Popper Oxides (La1–XSrx)2MO4±δ (M = Co, Ni, Cu). *J. Phys. Chem. Lett.* **2016**, *7* (10), 1939–1944. https://doi.org/10.1021/acs.jpclett.6b00739.

(66) Hu, X.; Li, M.; Xie, Y.; Yang, Y.; Wu, X.; Xia, C. Oxygen-Deficient Ruddlesden-Popper-Type Lanthanum Strontium Cuprate Doped with Bismuth as a Cathode for Solid Oxide Fuel Cells. *ACS Appl. Mater. Interfaces* **2019**. https://doi.org/10.1021/acsami.9b05445.

(67) Zhou, J.; Chen, G.; Wu, K.; Cheng, Y. Interaction of La2NiO4 (100) Surface with Oxygen Molecule: A First-Principles Study. *J. Phys. Chem. C* **2013**, *117* (25), 12991–12999. https://doi.org/10.1021/jp403094x.

(68) Barcellos, D. R.; Coury, F. G.; Emery, A.; Sanders, M.; Tong, J.; McDaniel, A.; Wolverton, C.; Kaufman, M.; O'Hayre, R. Phase Identification of the Layered Perovskite CexSr2- XMnO4 and Application for Solar Thermochemical Water Splitting. *Inorg. Chem.* **2019**, *58* (12), 7705–7714. https://doi.org/10.1021/acs.inorgchem.8b03487.

(69) Muñoz-García, A. B.; Ritzmann, A. M.; Pavone, M.; Keith, J. A.; Carter, E. A. Oxygen Transport in Perovskite-Type Solid Oxide Fuel Cell Materials: Insights from Quantum Mechanics. *Acc. Chem. Res.* **2014**, *47* (11), 3340–3348. https://doi.org/10.1021/ar4003174.

(70) Ritzmann, A. M.; Dieterich, J. M.; Carter, E. A. Density Functional Theory + U Analysis of the Electronic Structure and Defect Chemistry of LSCF (La0.5Sr0.5Co0.25Fe0.75O3−δ). *Phys. Chem. Chem. Phys.* **2016**, *18* (17), 12260–12269. https://doi.org/10.1039/c6cp01720g.

(71) Xu, S.; Jacobs, R.; Morgan, D. Factors Controlling Oxygen Interstitial Diffusion in the Ruddlesden–Popper Oxide La2–XSrxNiO4+δ. *Chem. Mater.* **2018**, *30* (20), 7166–7177. https://doi.org/10.1021/acs.chemmater.8b03146.

(72) Routbort, J. L.; Rothman, S. J.; Flandermeyer, B. K.; Nowicki, L. J.; Baker, J. E. Oxygen Diffusion in La 2− x Sr x CuO 4− Y. *J. Mater. Res.* **1988**, *3* (1), 116–121. https://doi.org/10.1557/JMR.1988.0116.

(73) Tealdi, C.; Ferrara, C.; Mustarelli, P.; Islam, M. S. Vacancy and Interstitial Oxide Ion Migration in Heavily Doped La 2-XSr XCoO 4±δ. *J. Mater. Chem.* **2012**, *22* (18), 8969–8975. https://doi.org/10.1039/c2jm30769c.